Check for updates

Controllable growth of MoS$_2$ nanosheets on TiO$_2$ burst nanotubes and their photocatalytic activity†

Qiushi Jiang,‡[a] Shang Wang,‡[a] Xue Li,[b] Zhaolian Han,[a] Chunli Zhao, [ID] *[c] Tingting Di,[d] Siyuan Liu[a] and Zhiqiang Cheng [ID] *[a]

MoS$_2$ nanosheets were grown on TiO$_2$ nanotubes by the simple hydrothermal method for the first time. The layer-by-layer growth of MoS$_2$ nanosheets led to a significant increase in the specific surface area of TiO$_2$/MoS$_2$ burst tube composites compared with TiO$_2$ burst tubes, a significantly enhanced ability to separate photo-induced carriers, and synergistic adsorption and visible light catalytic activity of dye molecules. The maximum adsorption (q_{max}) of MB was 72.46 mg g^{-1}. In addition, 94.1% of MB could be degraded after 30 minutes of visible light irradiation. The microsurface morphology, structure, chemical composition, element valence and band width of TiO$_2$/MoS$_2$ nanocomposites were analyzed by scanning electron microscopy (SEM), transmission electron microscopy (TEM), energy dispersive X-ray spectroscopy (EDS), X-ray photoelectron spectroscopy (XRD), X-ray photoelectron spectroscopy (XPS), diffuse reflectance spectroscopy (DRS) and photoluminescence spectroscopy (PL). The mechanism of photocatalytic reaction was studied via free radical capture experiments.

1. Introduction

TiO$_2$ has a low price, non-toxicity, no secondary pollution, high photo-sensitivity and excellent ability to oxidize and decompose organic matter, and its processing is relatively mature.[1–3] However, TiO$_2$ can only use ultraviolet light, which accounts for 4% of solar energy. Meanwhile, the rapid recombination of photogenerated electrons and holes in the reaction process also limits the photocatalytic efficiency of TiO$_2$, which greatly limits its wide application.[4–7] In the previous study, TiO$_2$ burst nanotubes (TiO$_2$NBTs) were prepared by combining electrospinning and dipping calcination. Compared with TiO$_2$ nano-fiber tubes, TiO$_2$NBTs have larger specific surface area and more pore structure.[8]

The band bending at the catalyst interface due to the composite of other nanomaterials provides a driving force for the separation of photogenerated electrons and holes, thus reducing the influence of carrier recombination and improving the photocatalytic activity.[9–12] For example, precious metals Pt,

Ru, Rh, Au and Ag and their corresponding oxides are common cocatalysts.[13–15] However, these materials are expensive and scarce, making it difficult to scale up. Strategies have been proposed to replace precious metals with cheap nanocrystalline materials,[16–31] and the semiconductor MoS$_2$ is one of the hot options,[32] which has a layered structure similar to graphene, anisotropy, chemical inertia, electron transfer rate, photo-resistance[33] and specific optical properties,[34] and is also a catalyst for dehydrogenation of complex hydrocarbons. Since the conduction band of MoS$_2$ is below the conduction band of anatase TiO$_2$, and the valence band exceeds that of anatase TiO$_2$, TiO$_2$ can transfer photoelectrons and holes to MoS$_2$, and its narrow band gap causes the photocatalyst complex of MoS$_2$ and TiO$_2$ to broaden the wavelength absorption range and reduce the recombination rate of photoexcited electron–hole pairs. A large number of studies have proved that the combination of MoS$_2$ and TiO$_2$ as a transition metal sulfide can improve the activity of photocatalyst.[35–39] However, most of them modify MoS$_2$ on the surface of TiO$_2$ nanofiber[40–43] and its array[44,45] as well as nano–microspheres,[46,47] and the composite structure between TiO$_2$ burst nanotubes matrix and MoS$_2$ with special morphology has not been described. As we all know, the performance of photocatalysts largely depends on their morphologies. Therefore, it is of great significance to prepare nanocomposites with multiple catalytic active sites and stable morphology and to further explore their catalytic mechanisms.[48–51]

In this paper, TiO$_2$/MoS$_2$ burst nanotube composites were easily synthesized on TiO$_2$ burst nanotubes by hydrothermal method. The uniform growth of MoS$_2$ nanosheets on TiO$_2$ burst

[a]College of Resources and Environment, Jilin Agricultural University, Changchun 130118, People's Republic of China. E-mail: czq5974@163.com

[b]College of Information Technology, Jilin Agricultural University, Changchun 130118, People's Republic of China

[c]College of Horticulture, Jilin Agricultural University, Changchun 130118, People's Republic of China. E-mail: zcl8368@163.com

[d]Northeast Electric Power Design Institue Co.,LTD. of China Power Engineering Consulting Group, Changchun 130021, People's Republic of China

† Electronic supplementary information (ESI) available. See DOI: 10.1039/d0ra08421b

‡ Qiushi Jiang and Shang Wang contribute to the work equally.

tubes not only maintains the structural stability, but also achieves rapid electron transfer through close contact between TiO_2 and MoS_2. The uniform layer by layer growth of MoS_2 nanosheet results in a larger exposed surface and more porous structure of TiO_2/MoS_2 nanotube burst composite, which enhances the photocatalytic activity driven by UV-vis while maintaining the structural stability. During the catalytic degradation of MB, relative to TiO_2 burst tubes and hydrothermal MoS_2 nanosheets, the ability of TiO_2/MoS_2 burst nanotube composites to adsorb MB dye molecules and separation of photoinduced carriers is greatly enhanced. Under visible light irradiation, MB solution is completely degraded within 70 min, thus improving the utilization efficiency of solar energy.

2. Experimental

2.1 Materials

Polystyrene (PS) was provided by Shanghai Youngling Electromechanical Technology Co., Ltd (the PS with M_w = 150 000 g mol^{-1}). Tetrabutyl titanate (TBOT 97%), N,N-dimethylformamide (DMF), methylene blue (MB), benzoquinone (BQ), and isopropanol (IPA) and triethanolamine (TEA) were purchased from Aladdin Industrial Corporation. Absolute ethanol, oxalic acid ($H_2C_2O_4$), glucose, sodium molybdate ($Na_2MoO_4 \cdot 2H_2O$) and thiourea (CSN_2H_4, 99%) were bought from Beijing chemical works. All chemicals were of analytic grade and without further purification.

2.2 Preparation of TiO_2 burst nanotubes

The preparation of TiO_2 burst tube has been described in our previous work, weighing 1.15 g PS and 2.85 g DMF, and then adding oxalic acid (0.3 wt%) to the mixture. The spinning precursor solution was prepared by stirring the mixture at 60 °C for 6 h. PS fibers are manufactured using electrospinning equipment with a high voltage power supply, rotary nozzles and grounded collectors. When the ambient temperature is 25 °C and the ambient humidity is 30%, transfer the spinning solution to the syringe and connect it to the 14 kV high voltage power supply. The flow rate of the spinning solution was controlled at 1.0 mL h^{-1}, and the distance between the needle and the receiver was 16 cm to obtain electrospun nanofiber membrane. The collected nanofiber membrane was fully immersed in TBOT ethanol solution with a mass ratio of 1 : 10 for 15 min, and then taken out. After the soaking process, the composite membranes were dried in an oven at 60 °C for 1 h. Finally, the dried PS/TBOT fiber membrane was calcined at a heating rate of 3 °C min^{-1} to 550 °C in a tube furnace, and kept 30 min. Naturally cool after annealing to obtain TiO_2 burst nanotubes.[8]

2.3 Preparation of TiO_2/MoS_2 nanocomposite by hydrothermal method

First, 0.2 g sodium molybdate and 0.4 g thiourea were dissolved in 30 mL glucose solution (0.05 M), and then 100 mg TiO_2 burst nanotubes and the above mixed solution were simultaneously transferred to a 50 mL polytetrafluoroethylene lined stainless steel autoclave, which was then placed in an oven at 200 °C for 24 h. After the autoclave was naturally cooled, the black products were collected by centrifugation and washed with ethanol for 3–5 times. The washed composites were dried overnight in the oven at 60 °C to obtain TiO_2/MoS_2 burst nanotube composites. As a contrast, a single MoS_2 nanosheet was prepared, and the amount of material used in the hydrothermal process was exactly the same as that in the preparation of TiO_2/MoS_2 nanocomposites, except that no TiO_2 burst nanotubes were added.

2.4 Characterization

The surface morphology of the sample was observed by scanning electron microscope (SSX-550, Shimadzu). The EDS mapped image and microstructure of the samples were observed by transmission electron microscope (TEM, TecnaiF20) of energy dispersive X-ray spectrometer (EDS). X-ray photoelectron spectroscopy (XPS, VGESCALABLKII) is used to determine the chemical composition of the complex. The specific surface area and pore diameter of the samples were analyzed using a specific surface & pore size analysis instrument (BET, 3H-2000PS1, BeishideInstrument). The crystal structure of the sample can be determined by X-ray diffractometer (XRD, XRD-7000, Shimadzu). The absorption characteristics of the samples and the absorptivity of degraded dyes were studied by UV-vis spectrophotometer with integrating sphere (TU-1950, Beijing Purkinje Corporation). The photoluminescence (PL) spectrum excited by 325 nm wavelength was measured at room temperature on a fluorescence spectrophotometer (F-4500, Hitachi, Japan).

2.5 Organic adsorption characterization

As a common industrial dye and fungicide, MB has low biodegradability in water. In this work, methylene blue (MB) was used as a simulated organic pollutant to evaluate the adsorption properties of TiO_2/MoS_2 nanocomposites. The solution of 10 mg L^{-1}, 20 mg L^{-1}, 30 mg L^{-1}, 40 mg L^{-1}, 50 mg L^{-1} and 60 mg L^{-1} MB were put into the quartz tubes. 10 mg TiO_2 burst nanotubes, MoS_2 nanosheets and TiO_2/MoS_2 nanocomposites were added to each quartz tube. The suspension was magnetically stirred in the dark for 24 hours, and 3 mL solution was extracted from it for centrifugation to measure the absorbance value of the solution.

2.6 Photocatalytic test

The photocatalytic activity of TiO_2/MoS_2 nanocomposites was studied by the degradation of MB solution under visible light. First, the nanocomposites of 10 mg were mixed with the 60 mL (10 mg L^{-1}) MB solution and stirred by magnetic force in dark for 30 minutes to achieve the adsorption–desorption equilibrium. Then the mixed solution was irradiated with the visible band of a mercury lamp (360 W), and the distance between the solution and the light source was 10 cm. What's more, the irradiation power used for photocatalysis was 450 mW cm^{-2}. The UV-vis absorption spectrum can be measured when the 3 mL solution is taken with a filter after each 10 min irradiation of UV-vis, and a blank control test is carried out.
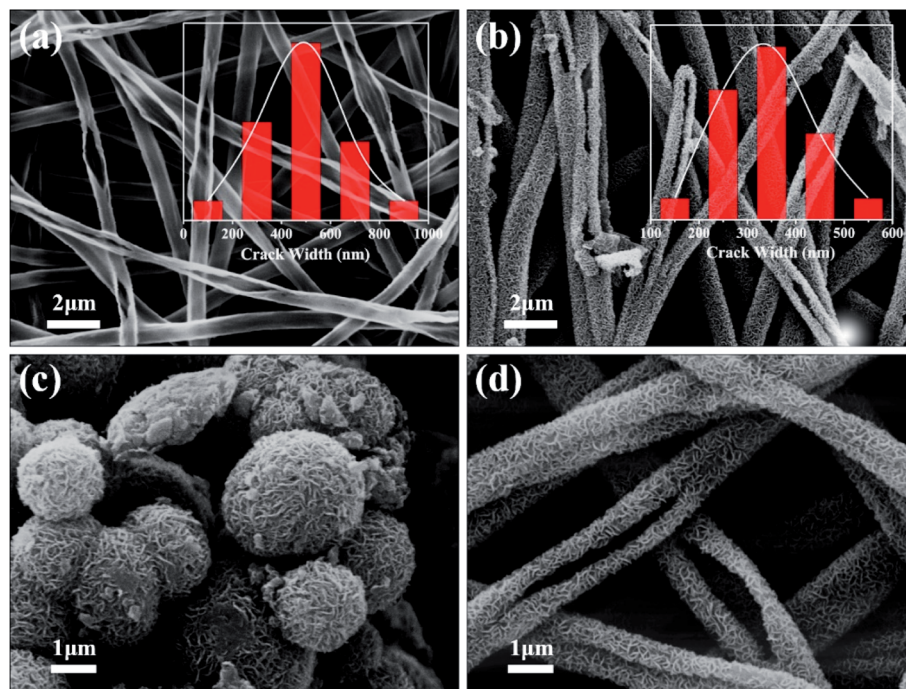
Fig. 1 SEM images of TiO$_2$ burst nanotubes (a) and TiO$_2$/MoS$_2$ nanocomposite (b), MoS$_2$ nanosheets (c) and TiO$_2$/MoS$_2$ nanocomposite (d) at the same multiple. (The illustrations in (a) and (b) are the cracking degree map of TiO$_2$ burst nanotubes and TiO$_2$/MoS$_2$ nanocomposite, respectively.)
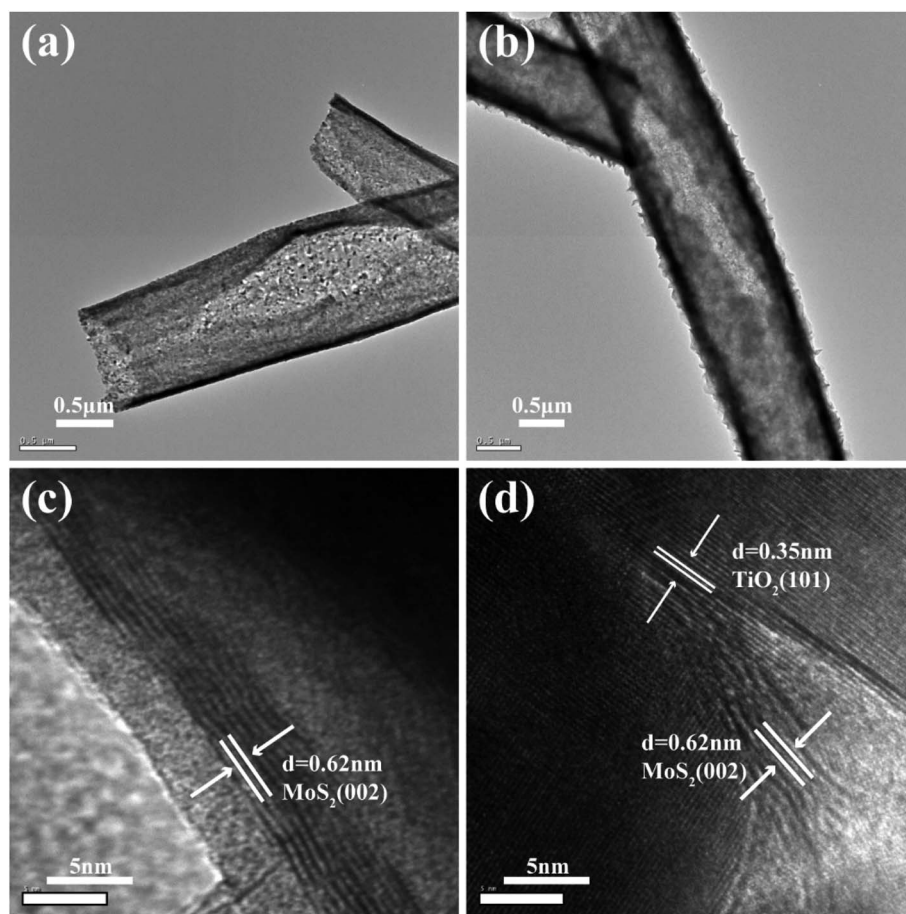

Fig. 2 TEM image of the TiO$_2$ burst nanotubes (a) TiO$_2$/MoS$_2$ nanocomposite (b), HRTEM images of several MoS$_2$ nanosheets (c) and TiO$_2$/MoS$_2$ nanocomposite (d).

2.7 Possible mechanism of photocatalytic activity

In order to explore the charge transfer process of TiO_2/MoS_2 nanocomposites during photocatalytic degradation, free radical capture experiments of different scavengers were carried out. The effects of superoxide radical ($\cdot O_2^-$), hydroxyl radical ($\cdot OH$) and hole (h^+) on the photodegradation of MB were investigated. Benzoquinone (BQ, 1 mM), isopropanol (IPA, 1 mM) and triethanolamine (TEA, 1 mM) were added to the reaction system as scavengers of $\cdot O_2^-$, $\cdot OH$ and h^+, respectively. The remaining steps were the same as those of photocatalysis test.

3. Results and discussion

Fig. 1(a) shows the TiO_2 burst nanotubes with a diameter of 600–1000 nm. Due to the gradual decomposition of oxalic acid with the increase of temperature in the calcination stage of PS/TBOT fiber membrane, CO_2 gas is released. Under the high temperature condition, CO_2 gas will leave tiny holes on the surface of TiO_2 nanotube when it escapes, and PS will degrade completely as a sacrificial template, causing disintegration of TiO_2 nanotubes and forming TiO_2 burst nanotubes. As shown in Fig. 1(b), after the MoS_2 nanosheets are composited on the TiO_2 burst nanotubes by a hydrothermal method, the diameter of the composite has also increased accordingly. However, by comparing Fig. 1(a) and (b), it is found that the cracking degree of the nanocomposite after the composite of MoS_2 and TiO_2 nanosheets is significantly smaller than that of the TiO_2 burst nanotubes. The reason is that MoS_2 nanosheets grow layer by layer at the position where the TiO_2 burst nanotubes. It is found that compared to the micron-scale irregular spherical agglomerates produced by the aggregation and growth of MoS_2 nanosheets without a growth template (Fig. 1(c)), the tiny holes provided by the TiO_2 burst nanotubes provide suitable nucleation sites for the growth of MoS_2 nanosheets. Moreover, in TiO_2/MoS_2 material, TiO_2 nano burst-tubes as basal hydrothermal preparation of TiO_2/MoS_2 overall still had a tubular cracking morphology, while MoS_2 combination in the form of three-dimensional layered nanometer sheets in both internal and external TiO_2 nano burst-tubes, improving the porosity of the composite material in general (Fig. 1(d)).

The morphological changes of the TiO_2/MoS_2 composite nano-burst tube materials were confirmed by TEM observations in Fig. 2(a) and (b). Typical layered structure MoS_2 particles were observed on the TiO_2/MoS_2 composite burst tube, while no layered structure MoS_2 were observed in the separate TiO_2 nano bursttubes catalyst. By measuring the HRTEM image of the MoS_2 nanosheets (Fig. 2(c)), the lattice spacing d is 0.62 nm, which corresponds to the hexagonal MoS_2 (002) plane (JCPDS37-1492). In the TiO_2/MoS_2 composite nanoburst tube material shown in (Fig. 2(d)), not only the hexagonal MoS_2 (002) plane can be detected, but also the (101) plane of anatase TiO_2 (JCPDS211272), and the lattice spacing d is 0.35 nm. Based on the above analysis, it is concluded that MoS_2 nanosheets grow on TiO_2 burst nanotubes through a simple hydrothermal reaction, and the two grow closely together. We believe that this composite heterostructure is beneficial to the transfer of photogenic charge carriers, and at the same time can enhance the charge separation ability and photocatalytic activity.
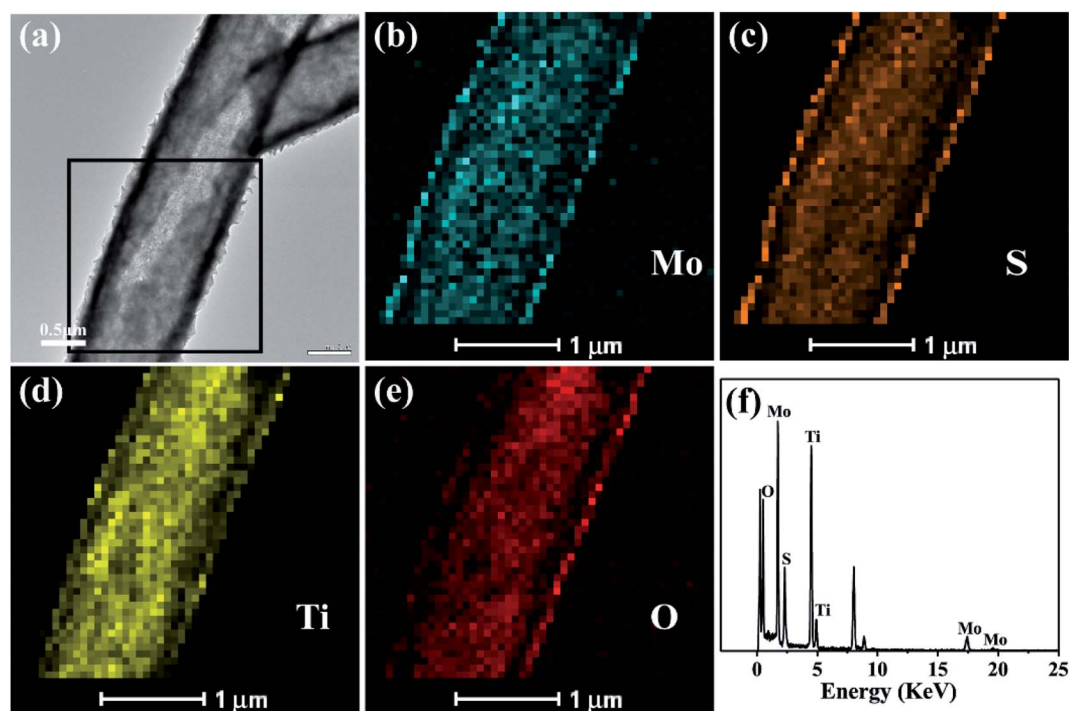

Fig. 3 TEM image (a) of the TiO_2/MoS_2 nanocomposite and TEM-EDS elemental mapping (b–e) of the selected area by black box in (a), EDS spectrum of the TiO_2/MoS_2 nanocomposite (f).
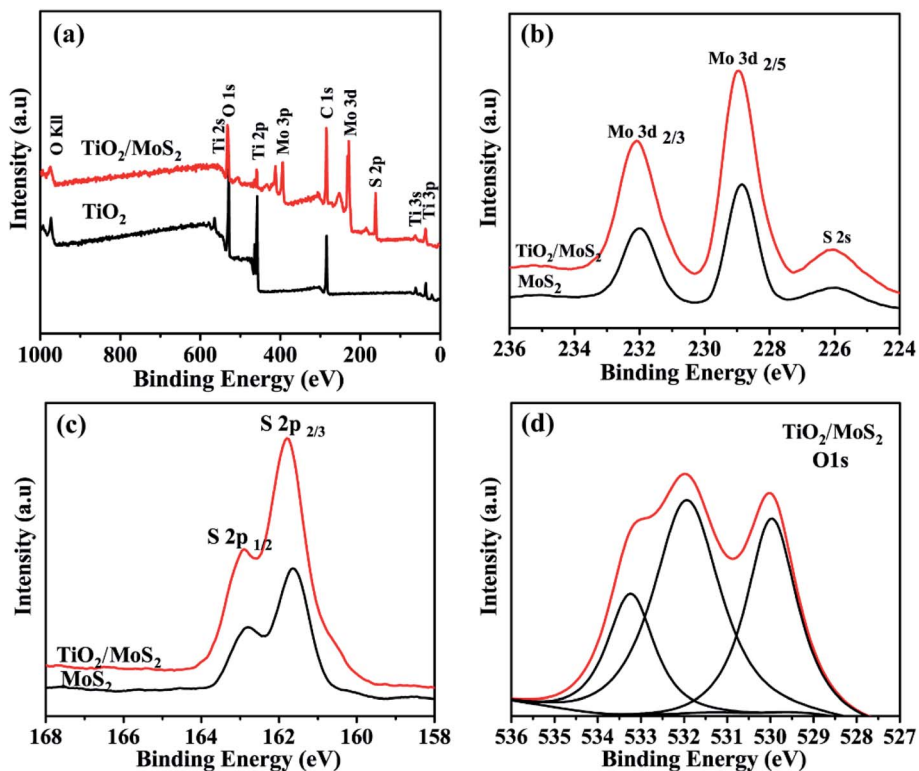
Fig. 4 XPS spectrum of the sample: (a) the full survey spectrum of TiO$_2$ and TiO$_2$/MoS$_2$, (b) Mo 3d peaks and (c) S 2p peaks of MoS$_2$ and TiO$_2$/MoS$_2$, respectively. (d) O 1s peaks of TiO$_2$/MoS$_2$.
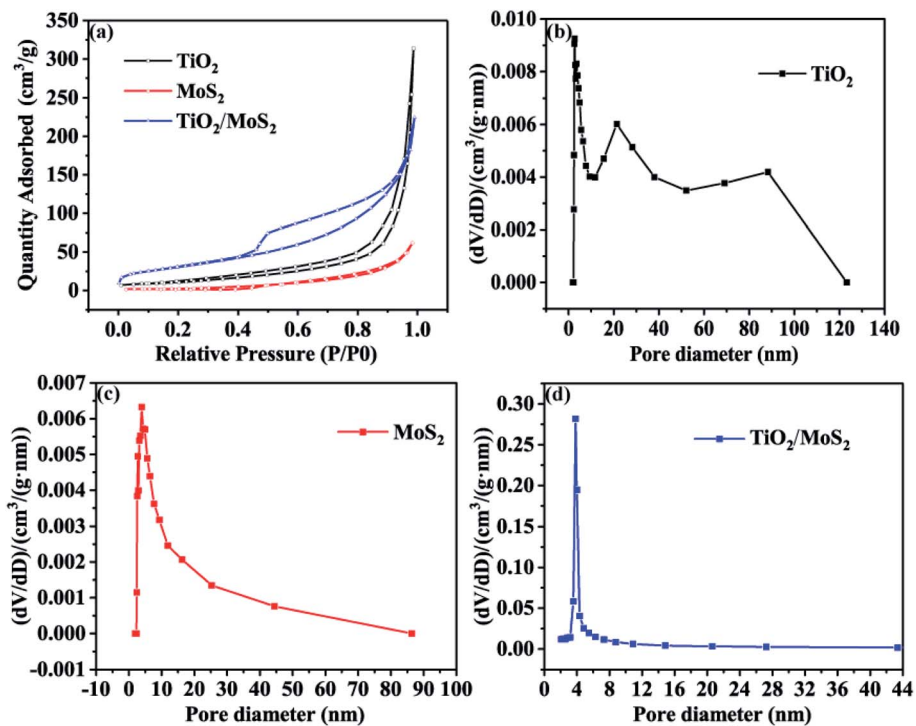

Fig. 5 Nitrogen adsorption–desorption isotherms (a) and BJH pore size distribution of three samples (b–d).

The elemental mapping analysis of energy dispersion-X-ray spectroscopy (EDX) of the black box for the selected area in Fig. 3(a) visually shows the distribution of Mo, S, Ti and O (Fig. 3(b)–(e)) in the TiO_2/MoS_2 composite burst tube. In Fig. 3(a), the cracked part can be clearly observed, while in Fig. 3(b) and (c), it can be observed that Mo and S completely cover the TiO_2 burst nanotubes. It can be seen that MoS_2 nanosheets grow uniformly on the inside and outside of the tube. Fig. 3(f), as the EDX spectrum of the TiO_2/MoS_2 composite, also detected all peaks representing Mo, S, Ti and O elements. The unlabeled peaks are derived from Cu and C in the carbon-coated copper grid. Besides, the calculated content of MoS_2 loaded on TiO_2 base was 71.7% (see the ESI†).

X-ray photoelectron spectroscopy ((XPS)) analysis is used to determine the chemical composition and bonding configuration of the prepared samples. The complete spectra of TiO_2 and TiO_2/MoS_2 (0–1000 eV) are shown in Fig. 4(a). As shown in Fig. 4(b) and (c), for pure MoS_2 nanosheets, the binding energies of Mo $3d_{3/2}$, Mo $3d_{5/2}$, S $2p_{1/2}$ and S $2p_{3/2}$ are 231.75 eV, 228.65 eV, 162.65 eV and 161.5 eV, respectively. When MoS_2 nanosheets were grown into TiO_2 burst nanotubes by hydrothermal synthesis, the binding energies of Mo $3d_{3/2}$, Mo $3d_{5/2}$, S $2p_{1/2}$ and S $2p_{3/2}$ peaks were converted to 231.7 eV, 228.6 eV, 162.55 eV and 161.4 eV, respectively, which were significantly lower than those of pure MoS_2 nanosheets. This transition means that there is an electronic interaction between TiO_2 burst nanotubes and pure MoS_2 nanosheets. As shown in Fig. 4(d),

the O 1s peak of TiO_2/MoS_2 complex, in addition to the peak value of 529.9 eV attributed to Ti–O–Ti bond, and the peak of 532.1 eV corresponds to the OH bond of water adsorbed on the surface. The peak of 531.75 eV cannot be observed in TiO_2 burst nanotubes, which may be related to the formation of Ti–O–Mo bond between MoS_2 nanosheets and TiO_2 burst nanotubes. Fig. S1† shows the O 1s peak of TiO_2 burst nanotubes, which is significantly different from that of TiO_2/MoS_2 composite.

The nitrogen adsorption–adsorption isotherms of the three samples are shown in Fig. 5(a). The isothermal curves of TiO_2 burst nanotubes and TiO_2/MoS_2 nanocomposites show typical adsorption–desorption behavior, indicating the existence of pores. Among them, the nitrogen absorption isotherm of TiO_2/MoS_2 nanocomposites shows a typical type IV adsorption isotherm with H3 hysteresis ring, which is the characteristic of mesoporous structure and slit pore. On the contrary, the adsorption–desorption curves of the pure MoS_2 nanowires almost coincide, indicating that the pores of pure MoS_2 nanosheets are very few. The specific surface areas of TiO_2 burst nanotubes, MoS_2 nanosheets and TiO_2/MoS_2 nanocomposites are 41.77, 10.59 and 113.97 $m^2 g^{-1}$, respectively (Table S1† compares the BET surface area and pore volume of the three samples). The existence of pore structure on TiO_2 burst nanotubes makes it easier for MoS_2 nanosheets to grow. Therefore, with the stacking growth of MoS_2 nanosheets, TiO_2/MoS_2 nanocomposites have more slit-like pores and larger specific surface area. As we all know, the specific surface area is an
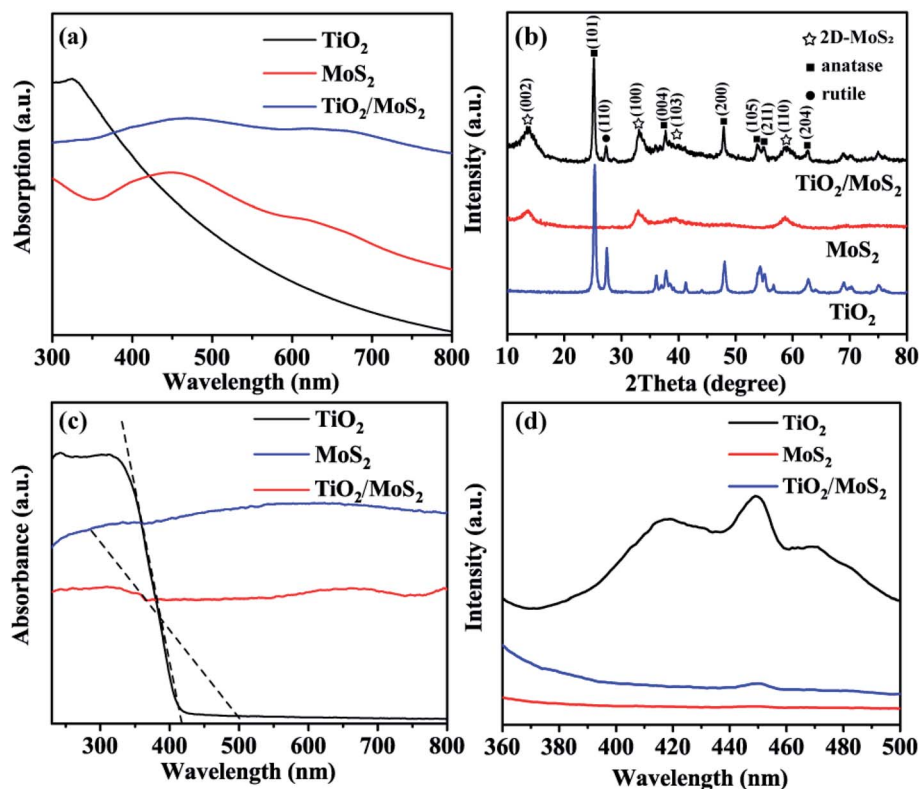

Fig. 6 Optical absorption spectra (a), XRD patterns (b), UV-vis diffuse reflectance spectra (c) and photoluminescence spectra (d) of the TiO_2 burst nanotubes, pure MoS_2 nanosheets and TiO_2/MoS_2 nanocomposite.

important property to study the photocatalytic activity of catalysts. In general, the larger specific surface area will lead to higher photocatalytic activity of the catalyst, because a larger surface area can provide more active sites. It can be seen from Fig. 5(b)–(d) that the pore diameter distribution of TiO_2 sample is relatively wide, basically 0–120 nm, and the pore size distribution of 0–120 nm TiO_2/MoS_2 is 0–90 nm. However, the pore diameter of TiO_2/MoS_2 composites is basically 0–8 nm. Compared with the other two single materials, TiO_2/MoS_2 composites have smaller pore size and larger specific surface area.

The UV-vis absorption spectra of solid dispersions of TiO_2 burst nanotubes, pure MoS_2 nanosheets and TiO_2/MoS_2 nanotube composites are shown in Fig. 6(a), TiO_2 burst tubes show significant absorption at less than 400 nm. Both MoS_2 nanosheets and TiO_2/MoS_2 nanotube composites have two absorption peaks in the region of 350–500 and 600–700 nm. However, the absorption in the visible region of TiO_2/MoS_2 nanoburst tube composites is obviously larger. As shown in Fig. 6(b), the main diffraction peaks of TiO_2 at $2\theta = 25.28°$, $37.80°$, $48.05°$, $53.89°$, $55.06°$ and $62.69°$ are in the directions of (101), (004), (200), (105), (211) and (204) respectively, corresponding to the anatase structure of TiO_2 (JCPDS 21-1272). While $2\theta = 27.45°$ corresponds to the direction of (110), which is the characteristic peak of rutile TiO_2 (JCPDS 21-1276). The diffraction peaks of pure MoS_2 at $2\theta = 13.6°$, $32.9°$, $39.2°$ and $58.7°$ correspond to (002), (100), (103) and (110) planes, respectively, which are hexagonal 2D-MoS_2 (JCPDS 37-1492). In addition, all the diffraction peaks of TiO_2 burst nanotubes and pure MoS_2 nanotubes can be found from the curves of TiO_2/MoS_2 burst nanotube composites, which fully demonstrates the growth of MoS_2 nanosheets on TiO_2 burst nanotubes, and the crystal structure of TiO_2/MoS_2 nanocomposites is similar to that of pure MoS_2, showing layered structure.

The optical properties of the samples were studied according to the UV-vis absorption spectrum in Fig. 6(c), As the absorption band of TiO_2 burst nanotubes slightly shifts out of the UV light region, which is consistent with the mixed structure of anatase and a small amount of rutile crystal form. According to the formula:

$$E_g = 1239.6/\lambda_g \tag{1}$$

It can be calculated that the band gaps of TiO_2 burst nanotubes and TiO_2/MoS_2 nanocomposite are 2.97 eV and 2.45 eV respectively. It shows that the excitation energy required by TiO_2/MoS_2 burst nanotube composite was lower than that of TiO_2 burst nanotube. Therefore, the growth of MoS_2 nanosheets on TiO_2 burst nanotubes is conducive to improve the degradation efficiency and visible light capture capability.

To evaluate the efficiency of charge trapping and photo-induced electron–hole pair recombination in semiconductor composites, Fig. 6(d) shows the photoluminescence (PL) spectra of TiO_2 burst nanotubes, MoS_2 nanosheets and TiO_2/MoS_2 nanocomposites. TiO_2 burst nanotubes have three main emission peaks. Among them, the peak at 417 nm (2.97 eV) corresponds to its near-forbidden band emission, while the other two peaks, 449 nm (2.76 eV) and 471 nm (2.63 eV), may be related to the defects related to the oxygen vacancy formed in the synthesis process. However, MoS_2 nanowires have no significant emission peak. Under the same test conditions, there is only one main luminescence peak in TiO_2/MoS_2 composites at 450 nm (2.75 eV). In general, PL emission is caused by the recombination of charged carriers, and the lower the emission intensity, the less the charge recombination.[52] Obviously, TiO_2 has the highest fluorescence intensity, which means the highest photogenerated electron–hole recombination. The fluorescence intensity of TiO_2/MoS_2 composite is lower than that of TiO_2 burst tube, indicating that the recombination of photogenerated electrons and holes is effectively suppressed. Therefore, TiO_2/MoS_2 can effectively promote the separation of photogenic carriers and prolong the separation time of photogenerated electron–hole pairs, thus showing excellent photocatalytic activity.

The adsorption performance is expressed by adsorption percentage (%) and adsorption capacity q_e (mg g^{-1}), which is calculated by eqn (2) and (3):

$$\text{Adsorption} = (C_0 - C_e)/C_0 \times 100\% \tag{2}$$
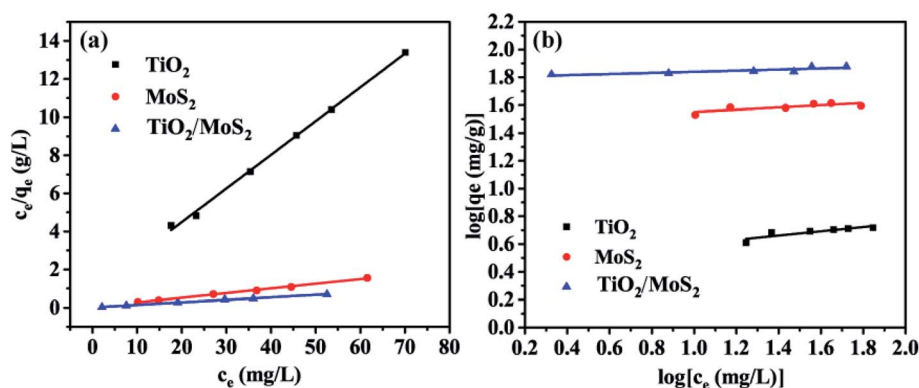
$$q_e = (C_0 - C_e) \times V/W \tag{3}$$

Fig. 7 Adsorption Langmuir (a) and Freundlich isotherms (b) of MB by different adsorbents: TiO_2 burst nanotubes, MoS_2 nanosheets and TiO_2/MoS_2 nanocomposite.

where C_0 is the initial concentration of organic pollution, C_e is its equilibrium concentration after adsorption, V is the volume of organic pollution solution (mL), and W is the weight of the synthesized adsorbent (mg). To describe how the adsorbate molecules interact with adsorbent, and the Langmuir and Freundlich isotherm equations were used to interpret the experimental adsorption data. The equations can be described as:

$$C_e/q_e = 1/K_L \times q_m + C_e/q_m \qquad (4)$$

$$\log q_e = \log K_F + \log C_e/n \qquad (5)$$

where q_e is the equilibrium adsorption capacity of adsorbent (mg g^{-1}), C_e is the equilibrium concentration of the dye (mg L^{-1}), q_m is the maximum amount of MB dye adsorbed (mg g^{-1}), K_L is the Langmuir constant which is related to the adsorption strength, K_F is the constant related to the adsorption capacity of the adsorbent (mg^{1-n} L^n g^{-1}), and n is the constant related to the adsorption intensity and adsorption capacity.

Fig. 7 shows the adsorption isotherm of the sample. The data were analyzed by Langmuir (Fig. 7(a)) and Freundlich (Fig. 7(b)) equations. The results show that when the concentration of MB solution is different, the correlation coefficients (R^2) of TiO$_2$ burst nanotubes, MoS$_2$ nanosheets and TiO$_2$/MoS$_2$ nanocomposites are 0.993, 0.996 and 0.997, respectively. Langmuir model can fit the experimental data well. However, the Freundlich curve fitting effect of the three samples is poor,

which is 0.734, 0.658 and 0.784 respectively. (Table S2:† adsorption parameters of THE Langmuir and Freundlich model for MB adsorption by TiO$_2$/MoS$_2$ nanocomposite.)

In the photocatalysis experiment, the degradation ability of TiO$_2$/MoS$_2$ nanocomposites was evaluated by degradation of MB solution. In Fig. 8(a) MB solution as a blank control degraded only a very small part under visible light irradiation. Before visible light irradiation, the dark adsorption experiment of 30 min was carried out to ensure that the sample reached the adsorption–desorption equilibrium. In the subsequent photocatalysis experiment, the photocatalytic efficiency of the samples was compared by showing the curve of relative concentration (C/C_0) as ordinate and irradiation time (t) as abscissa. Where C_0 is the initial concentration of MB solution and C is the concentration of MB solution at t. The dark adsorption results show that TiO$_2$/MoS$_2$ nanocomposites > pure MoS$_2$ nanosheets > TiO$_2$ burst nanotubes, which corresponds to the results of pore diameter distribution and specific surface area analysis. Under visible light irradiation, the dye removal rate of TiO$_2$ burst nanotube within 70 min was only 22.6%, this is because its absorption and utilization efficiency of visible light is not high, corresponding to the calculated band gap 2.97 eV. The pure MoS$_2$ nanometer sheet showed lower catalytic performance, with adsorption and degradation effect of about 50%. Due to the simultaneous crack, layered structure and the synergistic effect of anatase-rutile phase and hexagonal 2D-MoS$_2$, TiO$_2$/MoS$_2$ nanocomposites have the highest degradation efficiency of 96.7% in the reaction of 70 min because of their
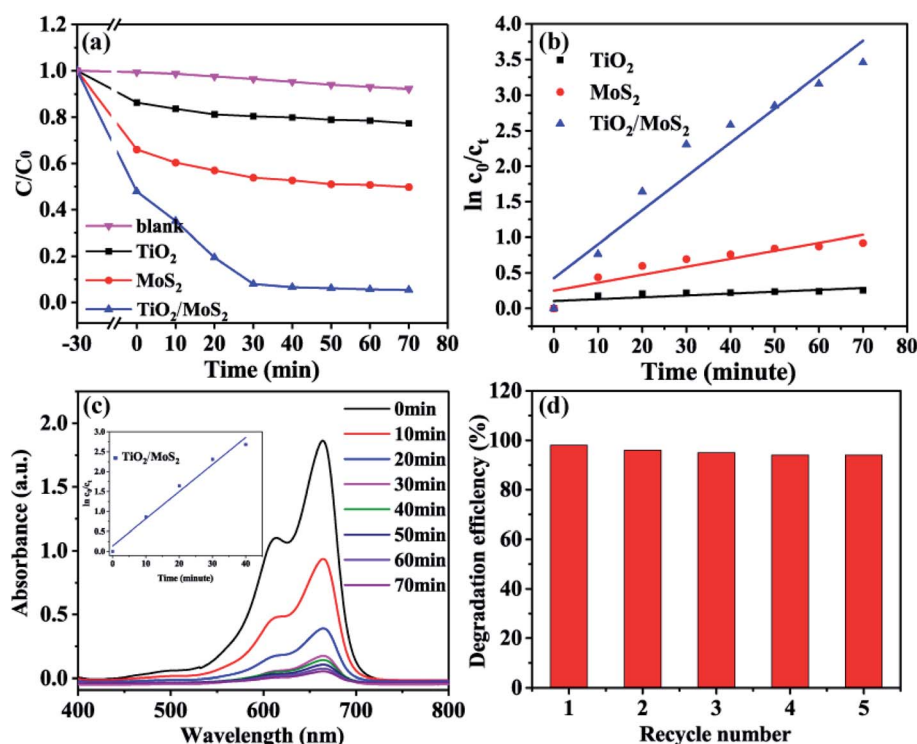

Fig. 8 Photocatalytic decomposing of MB under the visible light irradiation of the TiO$_2$ burst nanotubes, pure MoS$_2$ nanosheets and TiO$_2$/MoS$_2$ nanocomposite (a), the corresponding kinetic studies (b), the UV-vis absorption spectra for the photocatalytic degradation of MB in the presence of TiO$_2$/MoS$_2$ nanocomposite (c) and kinetic study of the first 40 min, the repeatability of five cycles of TiO$_2$/MoS$_2$ nanocomposite test (d).

Table 1 Photocatalytic performance of the materials developed in this study was compared with other recently reported TiO$_2$/MoS$_2$ composite nanostructured materials

Photocatalyst catalyst-dosage	Light source	MB dosage	Adsorption (%)	Degradation (%)	Time taken for degradation (min)	k	Ref.
50 mg TiO$_2$/MoS$_2$	400 W xenon lamp	100 mL (50 ppm)	Not mentioned	99	12	0.004 min^{-1}	50
50 mg TiO$_2$/MoS$_2$	30 W day lamp	100 mL (10 ppm)	Not mentioned	99	30	Not mentioned	54
20 mg TiO$_2$/MoS$_2$	250 W high-pressure mercury lamp	100 mL (4×10^{-5} M)	Not mentioned	94	60	0.048 min^{-1}	49
20 mg MoS$_2$/P25	500 W high-pressure mercury lamp	40 mL (10 ppm)	Not mentioned	80	5	0.253 min^{-1}	51
10 mg TiO$_2$/MoS$_2$	Sunlight	x mL (15 ppm)	63	96	25	Not mentioned	37
10 mg TiO$_2$/MoS$_2$	360 W high-pressure mercury lamp	60 mL (10 ppm)	72	94	30	0.068 min^{-1}	This work

large specific surface area, low band gap and visible light absorption capacity.

It can be seen from Fig. 8(b) that the degradation process of MB accords with the first-order kinetic reaction of Langmuir–HinShelwood, and the kinetic equation can be expressed as follows:

$$\ln C_0/C_t = k \times t \qquad (6)$$

the degradation rate constant of the sample (k, min^{-1}) is 0.0026, 0.0112 and 0.0477, respectively.

The results showed that TiO$_2$/MoS$_2$ nanocomposite had the highest constant degradation rate of MB. By dividing BET surface area (S_{BET}) by k_{MB} obtained by Langmuir–Hinshelwood first-order kinetic equation fitting, normalized rate constant of MB photodegradation (k'_{MB}) by pure TiO$_2$, pure MoS$_2$ and TiO$_2$/MoS$_2$ material was 7.18×10^{-5}, 1.04×10^{-3} and 4.21×10^{-4} min^{-1} m^{-2}, respectively.[53] It can be seen that the normalized rate constant of TiO$_2$/MoS$_2$ material was higher than that of pure TiO$_2$ material (see the ESI†).

According to Fig. 8(c), the absorption spectrum of the reaction solution decreases rapidly with the irradiation of visible light, and the degradation process of TiO$_2$/MoS$_2$ nanocomposites in the pre-40 min also consists with the first-order kinetic reaction of Langmuir–HinShelwood, with the degradation rate constant (k, min^{-1}) of 0.0681. 94.1% of MB dyes were degraded in the pre-30 min, which proved that the TiO$_2$/MoS$_2$ nanocomposites had excellent catalytic performance under visible light irradiation. In addition, in order to prove that the absorption spectrum decline in the solution under the action of TiO$_2$/MoS$_2$ nanocomposite was not caused by the increase in adsorption performance due to the changing visible light irradiation conditions. After the catalytic degradation experiment, the samples were recovered and desorbed with ethanol. The results showed that there was no methylene blue in the ethanol solution. Therefore, MB is not adsorbed by TiO$_2$/MoS$_2$ nanocomposites, but degraded under visible light. The cyclic degradation performance of TiO$_2$/MoS$_2$ nanocomposites to MB under visible light was studied, as shown in Fig. 8(d) (Fig. S1† shows the repeated utilization rate of TiO$_2$/MoS$_2$ nanocomposites). Moreover, with the increase of recycling times, the degradation efficiency of TiO$_2$/MoS$_2$ nanocomposites decreased slightly. After 5 times of reuse, the degradation rate of the samples was still 94% (Table 1).

Fig. 9 shows the comparison of the performance of TiO$_2$/MoS$_2$ nanocomposites for the degradation of MB dyes after adding different free radical scavengers, in which triethanolamine (TEA), benzoquinone (BQ) and isopropanol (IPA) have quenching effects on hole (h$^+$), superoxide anion radical ($\cdot$O$_2^-$) and hydroxyl radical ($\cdot$OH), respectively. The adsorption-analysis experiments in the dark showed that the addition of different traps had little effect on the adsorption properties of the composites. After visible light irradiation, the degradation rate of the samples without any free radical scavengers was the highest, reaching 94.2%. After adding BQ, the photodegradation rate decreased slightly to 90.6%. After adding IPA, the photodegradation rate of MB decreased obviously, and the
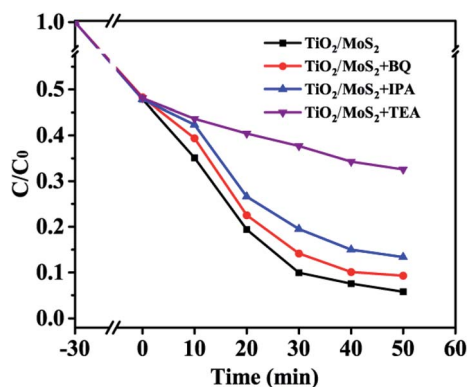
Paper

RSC Advances

Fig. 9 Photocatalytic degradation of MB over the TiO_2/MoS_2 nanocomposite photocatalyst with the addition of scavengers BQ, IPA and TEA.

degradation rate was reduced to 86.7%. In addition, after adding TEA into the reaction system, the catalytic activity of TiO_2/MoS_2 nanocomposites for the degradation of MB solution under visible light was significantly affected. Therefore, $\cdot OH$ and h^+ are the main active species in the visible light degradation of MB by TiO_2/MoS_2 nanocomposites, while $\cdot O_2^-$ has little effect on the degradation of MB.

Fig. 10(a) shows the sideband (VB, CB) positions of TiO_2 and TiO_2/MoS_2 nanocomposites, based on the band gap energy obtained in Fig. 6(c), band gaps can be obtained, using the empirical formulas,

$$E_{CB} = X - E_e - E_g/2 \tag{7}$$

$$E_{VB} = E_{CB} + E_g \tag{8}$$

where E_{CB} is the CB edge potential, E_{VB} is the VB edge potential, and X is the electronegativity of the semiconductor, which is the arithmetic mean of the electronegativity and the first ionization energy of the constituent atoms. E_e is the energy of free electrons on the hydrogen scale (about 4.5 eV), E_g is the band gap energy of semiconductors. The sideband position (VB, CB) of TiO_2 is 2.77 eV and −0.15 eV, respectively. The edge bands of TiO_2/MoS_2 nanocomposites are estimated by substituting the $X(TiO_2)$ value of matrix TiO_2, which is 2.52 eV and 0.07 eV,

respectively. Therefore, the growth of MoS_2 nanosheets on TiO_2 nanotubes can effectively reduce the band gap of the composites and the edge bands of the samples, and enables the TiO_2/MoS_2 nanometer composite material to have excellent photocatalytic performance under visible light.

Based on the above analysis, Fig. 10(b) presents the possible catalytic mechanism of TiO_2/MoS_2 nanocomposites under visible light irradiation. Because the band gap of MoS_2 nanowires is 2.40 eV,[48] it can absorb visible light whose wavelength is less than 653 nm. When the appropriate wavelength of light irradiates TiO_2/MoS_2 nanocomposites, the electrons (e^-) in the valence band absorb enough energy to transition to the conduction band and form holes (h^+) in the valence band. As the conduction band of MoS_2 is close to TiO_2, which accelerates the transfer of photoelectrons produced in TiO_2 to MoS_2, thus promoting the separation of carriers and reducing the recombination of photogenerated electrons and holes.[37] Since the CB potential (−0.38 V) of MoS_2 is more negative than the reduction potential of $O_2/\cdot O^{2-}$ (−0.33 V vs. NHE), e^- can effectively reduce the dissolved O_2 in the solution to $\cdot O^{2-}$ radical. Since the VB potential of TiO_2 (+2.77 V vs. NHE) is higher than the oxidation potential of $H_2O/\cdot OH$ (2.40 V vs. NHE), $\cdot OH$ will be thermodynamically formed on TiO_2.[16] On the special surface of TiO_2/MoS_2 burst tube nanocomposites, photogenerated electrons are quickly captured by oxygen molecules (O_2) in dye solution to form superoxide anions $(\cdot O_2^-)$. At the same time, holes (h^+) attack H_2O and OH^- in organic dye solution to form hydroxyl radical $(\cdot OH)$, resulting in strong oxidation, which can degrade organic dye molecules into environment-friendly H_2O, CO_2 and other compounds. The photocatalytic mechanism under visible light irradiation is as follows:
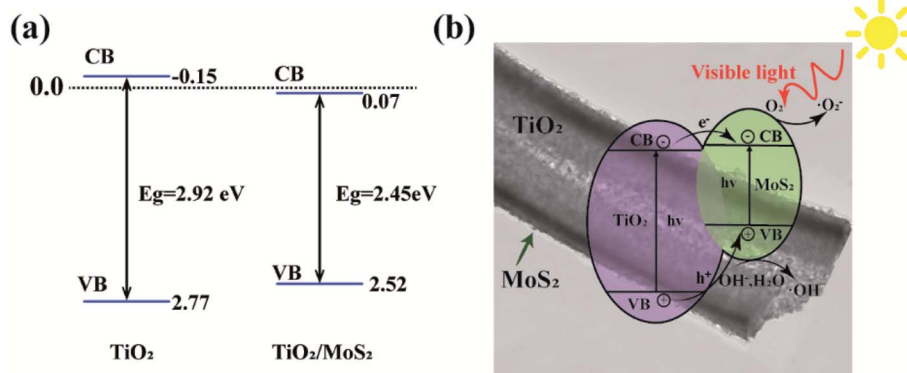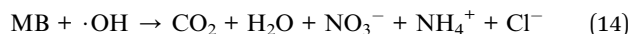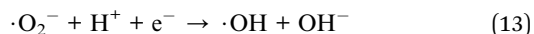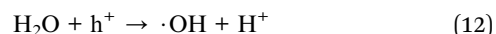
$$TiO_2/MoS_2 \rightarrow e^- + h^+(TiO_2/MoS_2) \tag{9}$$

$$O_2 + e^- \rightarrow \cdot O_2^- \tag{10}$$

$$OH^- + h^+ \rightarrow \cdot OH \tag{11}$$

$$H_2O + h^+ \rightarrow \cdot OH + H^+ \tag{12}$$

$$\cdot O_2^- + H^+ + e^- \rightarrow \cdot OH + OH^- \tag{13}$$

$$MB + \cdot OH \rightarrow CO_2 + H_2O + NO_3^- + NH_4^+ + Cl^- \tag{14}$$

Fig. 10 (a) Calculated band edge (VB, CB) position of TiO_2 and TiO_2/MoS_2 nanocomposite and (b) schematic diagram of charge separation and transfer of TiO_2/MoS_2 nanocomposite under visible light irradiation.

4. Conclusions

To sum up, TiO$_2$/MoS$_2$ nanocomposites show multi-functional synergistic properties of MB adsorption and visible light catalysis through low-cost hydrothermal preparation on the matrix of TiO$_2$ burst nanotubes. By characterization, the MoS$_2$ nanosheets grown on TiO$_2$ burst tubes had a layered composite structure, leading to a significant improvement in specific surface area (113.97 m^2 g^{-1}) compared with pure TiO$_2$ burst tubes (67.55 m^2 g^{-1}), and improved the pollutant adsorption capacity of the sample. The adsorption results of TiO$_2$/MoS$_2$ nanocomposite samples for MB were fitted with the Langmuir model, and the degradation process of MB under visible light accords with the first-order kinetic reaction of Langmuir–Hinshelwood. At the same time, the samples obtained high light capture ability and rapid electron transfer ability. The results of DRS detection calculation showed that the light absorption range of TiO$_2$/MoS$_2$ shifted to visible light, and the forbidden band width decreased. Photocatalytic tests confirmed that the visible light catalytic performance of TiO$_2$/MoS$_2$ nanocomposites got significantly improved compared with single MoS$_2$ nanosheets and TiO$_2$ burst nanotubes. Moreover, free radical trapping experiments confirmed that when TiO$_2$/MoS$_2$ nanocomposites degraded MB, h$^+$ was the main reaction species, while $\cdot$O$_2^-$ and $\cdot$OH were secondary reaction species.

The improvement of performance can be attributed to the larger specific surface area and more pore structure of TiO$_2$ burst nanotubes compared with TiO$_2$ nanotubes, which limits the aggregation of MoS$_2$ and retains exposed active sites. In addition, the existence of MoS$_2$ nanosheets increases the range of light absorption. Compared with single TiO$_2$ burst nanotubes and MoS$_2$ nanosheets, the heterojunction of TiO$_2$/MoS$_2$ burst nanocomposites is conducive to the effective transfer of carriers, thus improving the visible light catalytic activity.

This work confirmed the feasibility of the application of TiO$_2$/MoS$_2$ burst nanotube composites in the degradation of MB, and provided theoretical guidance and experimental basis for the synthesis of other burst nanotube semiconductor composites. We will devote ourselves to developing more application scenarios and exploring the scheme for large-scale preparation of the composite material.

Conflicts of interest

There are no conflicts to declare.

Acknowledgements

References

1 S. Zhu, J. Jiang, X. Zhang, Y. Liang, Z. Cui and X. Yang, *Mater. Des.*, 2017, **116**, 238–245.

2 F. Lu, J. Wang, X. Sun and Z. Chang, *Mater. Des.*, 2020, **189**, 108503.

3 R. Fagan, D. E. McCormack, S. Hinder and S. C. Pillai, *Mater. Des.*, 2016, **96**, 44–53.

4 V. Likodimos, *Appl. Catal., B*, 2018, **230**, 269–303.

5 J. Low, B. Cheng and J. Yu, *Appl. Surf. Sci.*, 2017, **392**, 658–686.

6 R. Qian, H. Zong, J. Schneider, G. Zhou, T. Zhao, Y. Li, J. Yang, D. W. Bahnemann and J. H. Pan, *Catal. Today*, 2019, **335**, 78–90.

7 M. Sachs, E. Pastor, A. Kafizas and J. R. Durrant, *J. Phys. Chem. Lett.*, 2016, **7**, 3742–3746.

8 S. Wang, Z. Han, T. Di, R. Li, S. Liu and Z. Cheng, *R. Soc. Open Sci.*, 2019, **6**(9), DOI: 10.1098/rsos.191019.

9 L. Zhang and M. Jaroniec, *Appl. Surf. Sci.*, 2018, **430**, 2–17.

10 B. Weng, M. Y. Qi, C. Han, Z. R. Tang and Y. J. Xu, *ACS Catal.*, 2019, **9**, 4642–4687.

11 T. S. Natarajan, K. R. Thampi and R. J. Tayade, *Appl. Catal., B*, 2018, **227**, 296–311.

12 J. Yi, X. Yuan, H. Wang, H. Yu and F. Peng, *Mater. Des.*, 2015, **86**, 152–155.

13 M. Diak, E. Grabowska and A. Zaleska, *Appl. Surf. Sci.*, 2015, **347**, 275–285.

14 M. Liu, J. Zhao, C. Xiao, Q. Quan and X. Li, *Mater. Des.*, 2016, **104**, 428–435.

15 S. Li, J. Cai, X. Wu and F. Zheng, *Appl. Surf. Sci.*, 2018, **443**, 603–612.

16 Y. H. Chiu, T. F. M. Chang, C. Y. Chen, M. Sone and Y. J. Hsu, *Catalysts*, 2019, **9**(5), DOI: 10.3390/catal9050430.

17 T. H. Do, C. Nguyen Van, K. A. Tsai, L. T. Quynh, J. W. Chen, Y. C. Lin, Y. C. Chen, W. C. Chou, C. L. Wu, Y. J. Hsu and Y. H. Chu, *Nano Energy*, 2016, **23**, 153–160.

18 P. Y. Hsieh, Y. H. Chiu, T. H. Lai, M. J. Fang, Y. T. Wang and Y. J. Hsu, *ACS Appl. Mater. Interfaces*, 2019, **11**, 3006–3015.

19 Y. S. Chang, M. Choi, M. Baek, P. Y. Hsieh, K. Yong and Y. J. Hsu, *Appl. Catal., B*, 2018, **225**, 379–385.

20 J. M. Li, C. W. Tsao, M. J. Fang, C. C. Chen, C. W. Liu and Y. J. Hsu, *ACS Appl. Nano Mater.*, 2018, **1**, 6843–6853.

21 Y. H. Chiu and Y. J. Hsu, *Nano Energy*, 2017, **31**, 286–295.

22 C. N. Van, T. H. Do, J. W. Chen, W. Y. Tzeng, K. A. Tsai, H. Song, H. J. Liu, Y. C. Lin, Y. C. Chen, C. L. Wu, C. W. Luo, W. C. Chou, R. Huang, Y. J. Hsu and Y. H. Chu, *NPG Asia Mater.*, 2017, **9**, e357.

23 X. Wang, S. Zhang, B. Peng, H. Wang, H. Yu and F. Peng, *Mater. Lett.*, 2016, **165**, 37–40.

24 K. A. Tsai and Y. J. Hsu, *Appl. Catal., B*, 2015, **164**, 271–278.

25 M. Y. Chen and Y. J. Hsu, *Nanoscale*, 2013, **5**, 363–368.

26 Y. F. Lin and Y. J. Hsu, *Appl. Catal., B*, 2013, **130–131**, 93–98.

27 Y. C. Chen, Y. C. Pu and Y. J. Hsu, *J. Phys. Chem. C*, 2012, **116**, 2967–2975.

28 Y. H. Chiu, T. H. Lai, M. Y. Kuo, P. Y. Hsieh and Y. J. Hsu, *APL Mater.*, 2019, **7**, 080901.

29 C.-W. T. Y.-J. H. Mei-jing Fang, *J. Phys. D: Appl. Phys.*, 2018, **51**, 404001.

30 P. Y. Hsieh, J. Y. Wu, T. F. M. Chang, C. Y. Chen, M. Sone and Y. J. Hsu, *Arabian J. Chem.*, 2020, **13**(11), 8372–8387.

31 M. Wang, Y. S. Chang, C. W. Tsao, M. J. Fang, Y. J. Hsu and K. L. Choy, *Chem. Commun.*, 2019, **55**, 2465–2468.

32 S. Harish, Prachi, J. Archana, M. Navaneethan, M. Shimomura, H. Ikeda and Y. Hayakawa, *Appl. Surf. Sci.*, 2019, **488**, 36–45.

33 Z. He, W. Que, Y. Xing and X. Liu, *J. Alloys Compd.*, 2016, **672**, 481–488.

34 S. Gu, M. Qin, H. Zhang, J. Ma, H. Wu and X. Qu, *CrystEngComm*, 2017, **19**, 6516–6526.

35 X. Chen, J. Zhang, X. Jiang, H. Wang, Z. Kong, J. Xi and Z. Ji, *Mater. Lett.*, 2018, **229**, 277–280.

36 X. Liu, X. Huo, P. Liu, Y. Tang, J. Xu, X. Liu and Y. Zhou, *Electrochim. Acta*, 2017, **242**, 327–336.

37 C. Wang, Y. Zhan and Z. Wang, *ChemistrySelect*, 2018, **3**, 1713–1718.

38 J. Zhang, L. Huang, Z. Lu, Z. Jin, X. Wang, G. Xu, E. Zhang, H. Wang, Z. Kong, J. Xi and Z. Ji, *J. Alloys Compd.*, 2016, **688**, 840–848.

39 A. Hamdi, L. Boussekey, P. Roussel, A. Addad, H. Ezzaouia, R. Boukherroub and Y. Coffinier, *Mater. Des.*, 2016, **109**, 634–643.

40 S. He, Y. Zhang, J. Ren, B. Wang, Z. Zhang and M. Zhang, *Colloids Surf., A*, 2020, **600**, 124900.

41 W. Zhou, Z. Yin, Y. Du, X. Huang, Z. Zeng, Z. Fan, H. Liu, J. Wang and H. Zhang, *Small*, 2013, **9**, 140–147.

42 R. Wei, X. Tian, Z. Hu, H. Zhang, T. Qiao, X. He, Q. Chen, Z. Chen and J. Qiu, *Opt. Express*, 2016, **24**, 25337.

43 Y. Li, Z. Wang, H. Zhao, X. Huang and M. Yang, *J. Colloid Interface Sci.*, 2019, **557**, 709–721.

44 J. Dong, J. Huang, A. Wang, G. V. Biesold-McGee, X. Zhang, S. Gao, S. Wang, Y. Lai and Z. Lin, *Nano Energy*, 2020, **71**, 104579.

45 L. Zheng, S. Han, H. Liu, P. Yu and X. Fang, *Small*, 2016, **12**, 1527–1536.

46 A. Balati, A. Matta, K. Nash and H. J. Shipley, *Composites, Part B*, 2020, **185**, 107785.

47 J. Su, S. Yu, M. Xu, Y. Guo, X. Sun, Y. Fan, Z. Zhang, J. Yan and W. Zhao, *Mater. Res. Bull.*, 2020, **130**, 110936.

48 W. Teng, Y. Wang, H. H. Huang, X. Li and Y. Tang, *Enhanced photoelectrochemical performance of MoS₂ nanobelts-loaded TiO₂ nanotube arrays by photo-assisted electrodeposition*, Elsevier B.V., 2017, vol. 425.

49 J. Zhang, L. Zhang, W. Yu, F. Jiang, E. Zhang, H. Wang, Z. Kong, J. Xi and Z. Ji, *J. Am. Ceram. Soc.*, 2017, **100**, 5274–5285.

50 M. Sabarinathan, S. Harish, J. Archana, M. Navaneethan, H. Ikeda and Y. Hayakawa, *RSC Adv.*, 2017, **7**, 24754–24763.

51 D. Wang, Y. Xu, F. Sun, Q. Zhang, P. Wang and X. Wang, *Appl. Surf. Sci.*, 2016, **377**, 221–227.

52 C. Liu, L. Wang, Y. Tang, S. Luo, Y. Liu, S. Zhang, Y. Zeng and Y. Xu, *Appl. Catal., B*, 2015, **164**, 1–9.

53 K. H. Chen, Y. C. Pu, K. Der Chang, Y. F. Liang, C. M. Liu, J. W. Yeh, H. C. Shih and Y. J. Hsu, *J. Phys. Chem. C*, 2012, **116**, 19039–19045.

54 K. H. Hu, Y. K. Cai and S. Li, *Adv. Mater. Res.*, 2011, **197–198**, 996–999.